Characterizing fault reactivation in shales with distributed fiber optic strain measurements in grouted boreholes

Chet Hopp[1], Yves Guglielmi[1], Antonio Pio Rinaldi[2,1], Florian Soom[1], Quinn Wenning[4], Paul Cook[1], Michelle Robertson[1], Maria Kakurina[5], and Alba Zappone[2,3]

[1]Lawrence Berkeley National Laboratory; Earth and Environmental Sciences Area, Berkeley, CA, USA
[2]Swiss Seismological Service, ETH Zürich, Zürich, Switzerland
[3]Department of Mechanical Engineering, ETH Zürich, Zürich, Switzerland
[4]Department of Earth Sciences, ETH Zürich, Zürich, Switzerland
[5]University of Neuchâtel, CHYN, Emile-Argand 11, 2000, Neuchâtel, Switzerland

Key Points:

- In response to a remote stress transfer, slip on a fault zone in a clay caprock concentrates at the upper and lower fault zone interfaces.
- Distributed strain sensing (DSS) shows equal measurand performance to standard borehole potentiometers, with better spatial resolution.
- DSS is sensitive to both borehole axial displacement and shear.

Corresponding author: Chet Hopp, `chopp@lbl.gov`

Abstract

Distributed fiber optic sensors are widely used for many geotechnical monitoring applications. One variety, Distributed Brillouin strain sensing (DSS), is sensitive to strain changes in a fiber optic core. While DSS has been used to measure strain inside a rock mass, these efforts have been limited to qualitative assessments. We present DSS measurements in six boreholes drilled across a fault zone in shale (Opalinus Clay), a cap-rock analog accessed from the ∼400 meter deep Mont Terri Underground Laboratory in Switzerland. We compare these data with co-located measurements of displacement from a chain potentiometer and a three-dimensional displacement sensor (SIMFIP). DSS is able to record in- and off-fault strain variations induced by a gallery excavated 30–50 m away, and by fluid injections at pressures of >4.5 MPa. During gallery excavation, the potentiometer and DSS both measure a total permanent displacement at the fault of ∼200 microns. DSS is sensitive to longitudinal and shear strain with measurements showing that fault shear is concentrated at the top and bottom interfaces of the fault zone with little deformation within the fault zone itself. The fluid injection test shows that a non-linearity of the DSS strain vs injection pressure curve occurs when reaching the fault opening pressure limit. This provides an approach to localizing fault opening along a borehole in time and space. Overall, our work demonstrates the fidelity and quantitative utility of DSS systems for fault zone hydromechanical monitoring while also presenting rare direct measurements of remotely-triggered fault slip.

1 Plain language summary

Understanding how and why faults move in different environments is important for a number of practical applications including geologic CO_2 sequestration, oil and gas exploration and production, geothermal energy exploitation, and forecasting induced seismicity. Here we show that fiber optic cables can be used to accurately measure fault slip when cemented inside boreholes that intersect such a structure. This allows monitoring of a larger volume of rock than ever before. Our measurements show that a kilometers-long fault in a clay rock, when disturbed by the excavation of a tunnel ∼30 m away, slipped mostly along its upper and lower interface. The excavation also produced slip on other, smaller fractures, with slip on these planes sometimes exceeding the slip on the larger fault. Direct measurements of slip on fractures and faults such as these will help us to answer questions like, “Will CO_2 or radioactive waste leak out of a reservoir/repository after we place it there?” or “What is the likelihood of triggering an earthquake during this injection operation on or near a fault?”

2 Introduction

A broad array of scientific and engineering applications have sprung up in the past few decades around the use of fiber optics as distributed measurement devices (so-called distributed fiber optic sensing, DFOS). These techniques leverage light that is scattered in the opposite direction of a passing optical pulse and, by measuring the frequency and gain of these backscattered components, can be used for sensing purposes. The result is a quasi-continuous sensor capable of being deployed in harsh environments and over distances of several kilometers (Hartog, 2017).

In this study we focus on measurements of the longitudinal strain of the sensing fiber through interrogation of the Brillouin component of backscattered light. Distributed Brillouin sensing (referred to here as distributed strain sensing, DSS) has found myriad applications since its inception in the 1990’s, mostly monitoring the state-of-health of various elements of critical infrastructure including the telecommunications fibers themselves (Tateda et al., 1990), the underground tunnels that house them (Naruse et al., 2005), nuclear waste repositories (Delepine-Lesoille et al., 2012), roads (Iten et al., 2008), levees (Naruse, 1999), and the stability of critical slopes (jun Wang et al., 2008).

Distributed fiber optics have also been deployed in deep boreholes, initially for monitoring of borehole casing integrity in oil and gas reservoirs (Zhou et al., 2010) but, more recently, downhole DSS has been used to monitor pumping-induced compaction (C.-C. Zhang et al., 2018), track the progression of hydraulic fractures in unconventional oil and gas reservoirs (Z. Zhang et al., 2020), and measure injection-induced strains in shallow aquifers (Sun et al., 2020). While these studies convincingly demonstrated the ability of DSS to measure strains on the order of tens of microstrains ($\mu\epsilon$), borehole-based measurements are inherently difficult to verify due to inaccessibility and the difficulty of locating separate instruments within a single borehole.

Two previous studies have made an attempt to ground truth DSS strain measurements in grouted boreholes. Krietsch et al. (2018) monitored a series of hydraulic stimulation tests in the Grimsel underground lab with co-located DSS and Fiber Bragg Gratings (FBGs). Using the FBG system as the 'true' measure, the authors determined that the DSS system provided good qualitative agreement with the FBG system but poor temporal and measurand resolution. They also observed poor agreement in the magnitude of the measured strains. Valley et al. (2012) grouted fibers into a sill pillar that was actively undergoing mining and attempted to corroborate the measurements using co-located extensometers. They also concluded that, while the DSS measurements were qualitatively in agreement with the extensometer, the measurements were not useful in quantifying the strain in the borehole. Both of these studies highlight the ongoing need for field testing and independent corroboration of DSS measurements in grouted boreholes.

In this study we present measurements from a suite of seven boreholes intersecting a fault, hereafter referred to as the Main Fault, in the Mont Terri Rock Laboratory (MTRL, Switzerland). These boreholes are part of an experimental setup aimed at studying the effect of CO_2 injection and pressurization (CS-D and FS-B projects; Zappone et al., 2020; Guglielmi et al., 2018) on the deformation and permeability of a fault zone affecting the Opalinus Clay, a low permeability rock considered an analog to a reservoir caprock (Bossart et al., 2017). Six of the seven boreholes are instrumented with a loop of single-mode fiber optic cable, grouted behind casing or anchored to inflatable packer assemblies. The boreholes also contain displacement sensors, including a chain potentiometer and a three-dimensional displacement sensor called the SIMFIP (Guglielmi et al., 2013), which are co-located with the fiber optic loops and allow us to tune our DSS measurements.

Our study details two instances of stress perturbation during which deformation was induced on the Main Fault: 1) A pulse-step injection experiment into the fault zone and 2) Excavation of a new gallery in the MTRL. First, we use these occurrences to demonstrate the sensitivity of our multi-borehole fiber array to the movement occurring within the Main Fault zone in response to disparate sources of stress perturbation. Thanks to the independent displacement measurements from co-located or proximal sensors with respect to the fibers, we demonstrate clear consistency between the strain magnitude and temporal occurrence captured between sensors. We discuss how a grouted fiber-behind-casing installation complements established methods. Second, we discuss the interest in continuous fiber-based measurements for detecting and characterizing fault reactivation and leakage in caprocks.

2.1 Fault activation experiments at the Mont Terri Rock Laboratory

The Mont Terri Rock Laboratory, operated by the Swiss Geological Survey, is located on one limb of a fault-bend anticline within a low-permeability claystone unit known as the Opalinus clay (Bossart et al., 2017; Hostettler et al., 2017). The Opalinus clay is both a potential target formation for Switzerland's nuclear waste repositories and a useful cap rock analog for CO_2 sequestration (Bossart et al., 2017). Additionally, the galleries of the MTRL are intersected by a kilometer-scale thrust fault zone, the so-called

Main Fault (Jaeggi et al., 2017), which offers researchers the opportunity to investigate the effect of fault activation on the leakage potential of a self-sealing clay unit (Guglielmi et al., 2017, 2020; Birkholzer, 2018; Zappone et al., 2020). The Mont Terri Main Fault consists of a thrust zone, 1 to 3 m in width, bounded by two major fault planes characterized by a strike of N066^o to N075^o and a dip of 45^o to 65^{o}SE (Figure 1). Deformations within the Main Fault are heterogeneous, including gouge, shear bands, folds, numerous centimeter-to-meter scale fault planes cutting the fault zone, and some ‘intact’ parts (Nussbaum et al., 2011; Wenning et al., 2020).

The CS-D and FS-B projects, directed by ETH Zürich and Lawrence Berkeley National Lab (LBNL), respectively, are focused on understanding how a minor fault affecting a clay unit (i.e. caprock) might respond to the long term injection of CO_2 (Zappone et al., 2020). The two projects are highly complementary. The CSD project is looking at small ∼0.05 ml/min injection of a CO_2 brine into the fault below the fault activation pressure. It is mainly focusing on long term hydro-mechanical and chemical processes of fluid diffusion at meter-scale in the fault zone (Zappone et al., 2020). The FS-B project is looking at large-scale (>5 L/min) injection into the fault above activation pressure. It is focused on hydromechanical processes at 10-meter scale during fault rupture, including the potential for induced seismicity, and during inter-rupture periods (Guglielmi et al., 2018).

A 70-m x 70-m x 70-m volume, crosscut by the Main Fault, is instrumented with 23 boreholes hosting various systems recording pressure and flow rate into multiple injection intervals, active and passive-source seismicity, electrical resistivity, fluid and gas geochemistry, and geomechanical strain/displacement/tilt. Figure 1 shows all boreholes drilled by CS-D/FS-B. Here we focus on the CS-D boreholes (colored in the foreground of Figure 1). The FS-B boreholes are shown in gray in the background.

3 Monitoring network considered in this study

In this study, we focus on instruments deployed in “Niche CO_2” of the MTRL (CS-D experiment), where seven boreholes have been drilled through the Main Fault zone (BCS-D1–7; Figure 1). BCS-D1 and BCS-D2 are the injection and fluid-monitoring boreholes, respectively, and are equipped with multi-level straddle-packer assemblies to enable the isolation of several depth intervals. Boreholes BCS-D3, D4, D5, and D6 are cased with PVC and house the electromagnetic and seismic monitoring systems (Zappone et al., 2020). Finally, BCS-D7 contains the SIMFIP instrument (Guglielmi et al., 2013), explained in greater detail below.

The depth of the Main Fault zone intersection with each borehole, as verified by image logging and core, varies from 11 to 28 m below the gallery floor (Table 1). The thickness of the fault zone varies between 1 and 3 meters within the MTRL and is characterized by a laterally heterogeneous mix of fault gouge, C’-type shear bands, meso- and micro-scale folds (Nussbaum et al., 2011). Here ‘scaly clay’ refers to a mass of unaltered, Opalinus microlithons, separated by slickensides, and is pervasive throughout the Main Fault (Jaeggi et al., 2017). Fault planes within the Main Fault zone are mostly oriented subparallel to the fault zone itself, but also include a set of conjugate fractures (Zappone et al., 2020; Wenning et al., 2020). In addition, a series of ENE-striking, bedding-parallel fractures, with similar strike but shallower dip than the Main Fault, are intersected by the CS-D boreholes (Zappone et al., 2020). Bedding in the Opalinus is oriented subparallel to the Main Fault, striking N055^o, and dipping SE046^o, roughly 15^o shallower than the Main Fault.

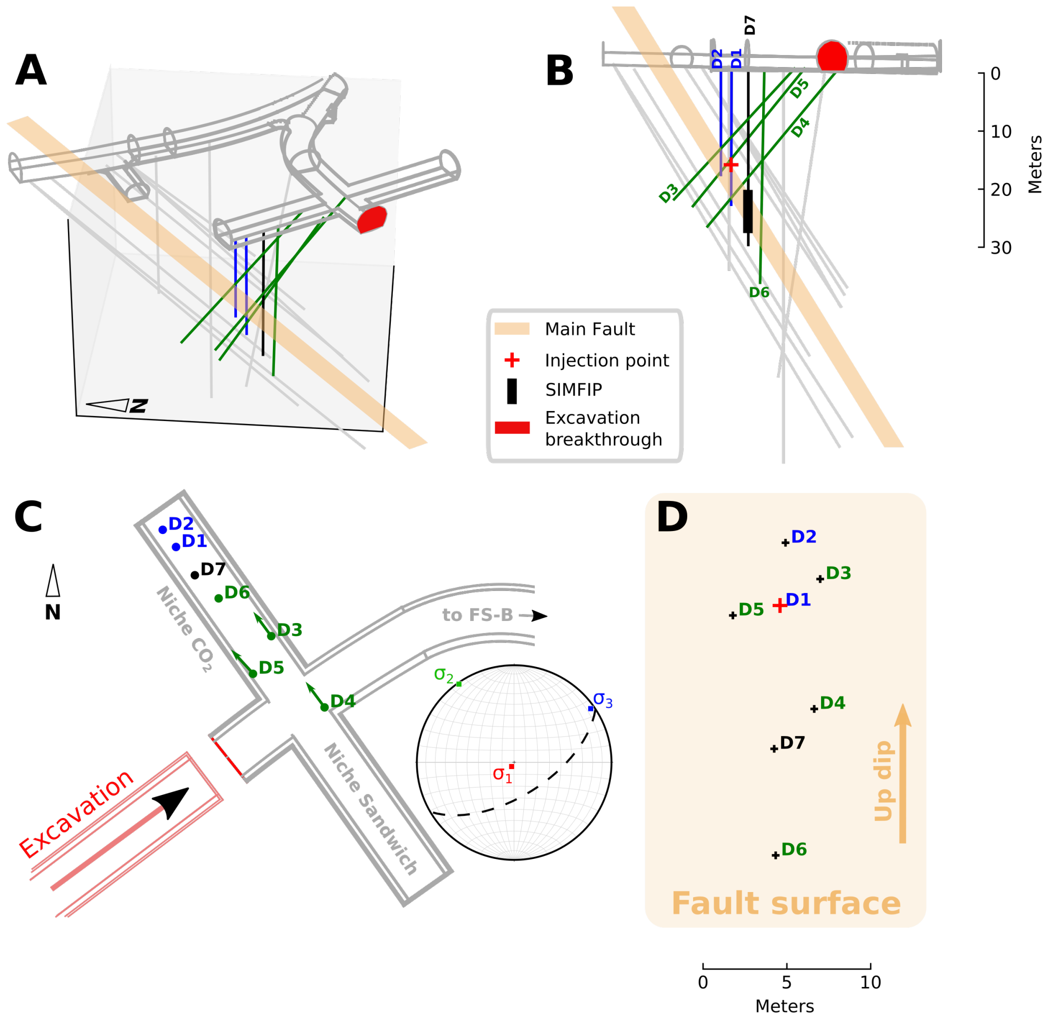

Figure 1. A) 3D perspective of the FS-B/CS-D project showing all boreholes colored by use. Blue boreholes D1 & D2 are injection and pressure monitoring boreholes, green boreholes contain monitoring systems, and the black borehole, D7, contains the SIMFIP displacement sensor. Light gray boreholes in the background are FS-B boreholes. All boreholes are instrumented with distributed fiber optic sensors except D7 B) Cross-section along Niche CO_2 with the injection point in D1 indicated by a red cross. C) Map view of the borehole collar locations in Niche CO_2 and lower hemisphere stereonet projection of the principal stress axes estimated by Guglielmi et al. (2020). Dotted line shows the approximate orientation of the Main Fault D) Intersection points for each well with the top of the Main Fault

Borehole name	Main Fault top [m]	Main Fault bottom [m]
BCS-D1	14.34	19.63
BCS-D2	11.04	16.39
BCS-D3	17.98	20.58
BCS-D4	27.05	28.44
BCS-D5	19.74	22.66
BCS-D6	28.5	31.4
BCS-D7	22.46	25.54

Table 1. Depths of the top and bottom of the Main Fault zone in each of the CS-D boreholes

3.0.1 Distributed fiber

Boreholes BCS-D1 through D6 contain a single 3.2 mm-diameter loop of BRUsens^{TM} strain sensing cable that itself comprises a single optical fiber hermetically sealed and strain-locked within a metal tube and an outer nylon sheath. These cables are designed to measure strains of up to 1% (10000 $\mu\epsilon$). In BCS-D1 and D2 (blue boreholes, Figure 1), the fiber optic cable (BRUSens 3.2 mm V4 metallic) is anchored by a compression ferrule at the top of each injection interval (with four and six intervals in D1 and D2, respectively). The straddle-packer assemblies allowed the fiber to pass through the injection interval and no grout was injected. This means that the fibers are in tension but not directly coupled to the host rock. Instead, they measure a combination of host rock deformation (e.g. fault opening leading to lengthening of the packer assembly) and injection system effects (for example, interval pressure changes due to inflation/deflation of the straddle packers themselves). This also means that, while the measurement in D1 and D2 is technically continuous, strain is essentially only measured over the intervals defined by the packer anchors, reducing the spatial resolution of the measurement.

In boreholes BCS-D3, D4, D5, and D6, the fiber (BRUSens 3.2 mm V9 grip) is cemented behind the PVC casing using a grout mix of 81.9 L water, 4.9 kg bentonite, and 50.1 kg cement (green boreholes, Figure 1). This provides a truly continuous measurement along the entire length of each borehole. In these cases, the nylon cable jacket is textured to provide optimized strain coupling between the fiber and the grout so that, in theory, only the grout strain is being measured, with the assumption made that the grout is coupled to the host rock. Each of these boreholes also includes a single resin 'plug' to mitigate against fluid traveling along the cemented annulus (Figure 2B). These plugs are 0.5–2 m thick sections where the resin replaces the grout in the annulus between the borehole wall and the PVC casing. Borehole diameter ranges from 101 to 146 mm, with consistent PVC casing diameters of 80 mm.

The fiber loops in each borehole are connected into multi-borehole loops and interrogated by an Omnisens DITEST temperature and strain unit using the Brillouin Optical Time Domain Analysis technique (Horiguchi & Tateda, 1989).

3.0.2 Potentiometer

A chain of 12 potentiometers is cemented behind casing alongside the fiber-optic loop in borehole BCS-D5 (Zappone et al., 2020; Rinaldi et al., 2020). Each potentiometer is connected to the adjacent units by a PVC tube and measures borehole axial displacement relative to the neighboring units with a maximum displacement of 100 mm. This chain of potentiometers provides a co-located measurement of displacement with respect to the optical fibers, allowing us to directly verify the measurements made with the DSS system.

3.0.3 SIMFIP

In borehole BCS-D7, a combined three-dimensional-displacement, pressure, and fluid electrical conductivity probe, the SIMFIP (Guglielmi et al., 2013), is clamped above and below the Main Fault. The clamps are 6.3 meters apart allowing the SIMFIP to measure the relative displacement across the entire Main Fault zone. The instrument uses six fiber-bragg gratings attached to a bespoke aluminum cage to resolve the full 3D displacement field with micrometer precision. Although the SIMFIP is alone in BCS-D7, and therefore is not co-located with any portion of the fiber optic loop, it offers the only three-dimensional fault displacement measurement with which to compare the DSS data.

4 Sources of stress perturbation

We focus on two types of stress perturbation at "Niche CO_2" (Figure 1). The range in potential strain between a gallery excavation and a pressure pulse-step injection test allows us to explore the range of strains that the DSS system is able to detect. In addition, we use these experiments to explore how the DSS can inform of fault activation modes.

4.0.1 Pressure pulse-step test

On 12 June 2019, the CS-D project conducted a pulse-step test (PST) as part of a series of hydraulic injection operations aimed at determining the fault opening pressure (FOP) of the Main Fault (Zappone et al., 2020). In this type of very low initial permeability clay fault, the FOP is the pressure at which injected fluids start consistently penetrating the fault. It is usually detected when the pressure applied in the test interval cannot stand a steady state. This test and all subsequent injections were into interval Q4 of BCS-D1 at the top of the Main Fault zone (depth 14.0–15.4 m; Figure 1). The PST is comprised of nine pressure steps beginning at ∼2.5 MPa and increasing in increments of 0.3 MPa. For each step the pump was turned on and then shut-in when the desired pressure was reached. The pressure was then allowed to decay freely for 10 minutes before beginning the next cycle. The final step, with a maximum Q4 interval pressure of 4.8 MPa, exceeded the FOP as indicated by the higher-amplitude pressure decay for the final step, after which the PST was concluded (Zappone et al., 2020). As the preceding step reached an interval pressure of 4.5 MPa without achieving opening, the FOP was inferred to be between 4.5 and 4.8 MPa.

4.0.2 Excavation of Gallery 18

On March 14 2018, excavation began on Gallery 18, a new ∼5 m diameter gallery expansion at the MTRL. Niche CO_2 was completed in May 2018, with installation of the CS-D systems occurring between August and December 2018. During the first half of 2019, the final stage of excavation proceeded towards Niche CO_2 as indicated in Figure 1. Excavation passed along the strike of the Main Fault at a constant ∼23 m distance from the upper fault zone interface. Breakthrough occurred adjacent to the CS-D experiment on 27 May 2019 (red faces in Figure 1). Prior to the breakthrough, movement was not detected by the DSS monitoring system at CS-D until 22 May 2019, when the excavation front was ∼26 m from the SIMFIP. We therefore focus on the period between 22 May and 3 June 2019.

5 Methods and processing

5.1 Distributed strain sensing

When a laser pulse is sent along an optical fiber, some amount of that light is scattered backwards by its interaction with changes in the refractive index of the fiber. There are three components of this backscattered light relevant to DFOS: one is elastic (Rayleigh) and two are inelastic (Raman and Brillouin). We are concerned here with the Brillouin component, which arises from an incident photon's interaction with crystal lattice vibrations that hold some of the optical fiber's heat. As the interaction is inelastic, the backscattered light is frequency shifted by some amount that linearly depends on the temperature and strain in the fiber. This relationship is described by Horiguchi and Tateda (1989) as:

$$\Delta\nu_B = \frac{\partial\nu_B}{\partial\epsilon}\Delta\epsilon + \frac{\partial\nu_B}{\partial T}\Delta T \tag{1}$$

where $\Delta\nu_B$ is the change in Brillouin frequency shift for given changes in strain, $\Delta\epsilon$, and temperature, ΔT. $\frac{\partial \nu_B}{\partial \epsilon}$ and $\frac{\partial \nu_B}{\partial T}$ are the strain and temperature change coefficients, respectively, which for this work are 500 MHz/% and 1.0 MHz/^{o}C.

Using Equation 1, the DITEST interrogator determines the combined temperature and strain contribution to the measured Brillouin frequency shift. Each measure is then related to a given point along the fiber by recording the launch and arrival time of the probe pulse with respect to the speed of light. Because the light pulse from the interrogator has a finite length, measurements are averaged over the corresponding length of fiber. This is referred to as the spatial resolution (or often the 'gauge length'). The Brillouin frequency shift for one gauge length is reported as a single measurement at a point along the fiber that we call a 'channel'. The spatial sampling and spatial resolution were 0.26 and 0.5-to-1.0 meters, respectively, for each of the periods of our study. Notice that the channel spacing is less than the spatial resolution. Therefore, the DSS measurement is a sliding window with a width equal to the spatial resolution, slid along the fiber in increments defined by the spatial sampling.

Because the Brillouin frequency shift is sensitive to both temperature and strain changes, a number of methods are employed to deconvolve their contributions. Often, an independent measurement of temperature (for example from a Raman scattering system) is used to remove the temperature contribution from the Brillouin measurements. Alternatively, a "strain free" cable is somehow decoupled from the system of interest and can be co-located with a coupled cable and connected in series. In our case we had access to neither, but we make the assumption that the temperature change within our testbed is negligible with respect to the changes in Brillouin shifts being measured (Madjdabadi et al., 2014, 2016; Hartog, 2017).

5.2 Borehole mapping and measurement symmetry

As mentioned above, for any given distributed strain measurement, its distance along the fiber is accurately known from the two way travel time in relation to the speed of light. Translating this distance into a borehole coordinate requires a process of 'mapping' whereby the distances along-fiber are matched to the known locations of the features we want to measure (in this case boreholes BCS-D1–D6). We decide to map distance to location by observing a single Brillouin frequency shift measurement along the entire fiber length (i.e. one time sample; Figure 2A). Because the fiber is installed as a loop in each borehole, we expect there to be symmetry in the measurements about the bottom of the boreholes. In other words, the downgoing and upgoing legs of the fiber in a given borehole should measure roughly the same strain.

For the case of our experiment (as noted in Section 3.0.1), the BRUsens cable is grouted into the boreholes (or attached to the casing above the packers in D1 and D2) while the sections of fiber between boreholes are standard patch cables lying in a cable tray along the gallery wall. The difference in fiber coating and installation produce an obvious difference in the Brillouin frequency measurement that allows us to map the along-fiber distances corresponding to the entry and exit points for each borehole. In Figure 2A, the entry and exit points for each borehole are indicated by dotted lines, with the bottom shown as a single solid line. The mapped along-fiber lengths agree with field measurements of the cable lengths set in the gallery. By manually selecting the point of greatest symmetry for each borehole and accounting for their known drilled depths, we isolate the slice corresponding to each borehole.

The process of borehole mapping should, in theory, result in two parallel sections (legs) of fiber in each borehole; one downgoing and one upgoing. Assuming that each is measuring approximately the same strain field, the measurements should be equal between up and down-going fiber for a given depth. Figure 2B shows both the down and up-going fiber leg in each borehole on 3 June 2019, following the breakthrough of the ex-

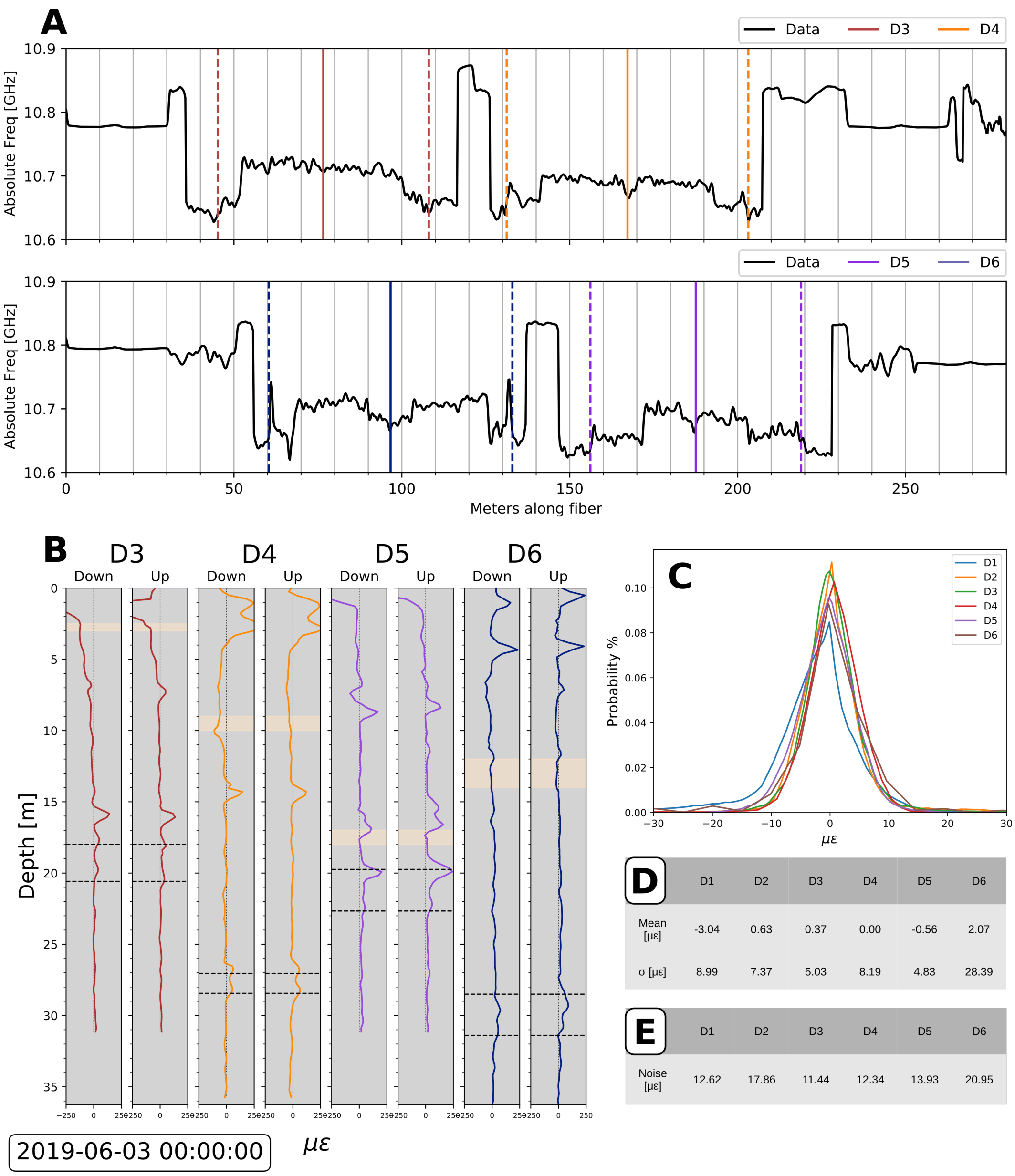

Figure 2. A) Absolute frequency along the length of the fiber during gallery excavation. The two panels correspond to two separate fiber optic loops, each with two boreholes. Boreholes D1 and D2 were added after excavation was completed. B) Distributed strains on the down and up-going leg of each on 3 June 2019, following the breakthrough of the excavation front on 27 May 2019. The depth to the Main Fault is marked with dotted lines, resin plugs are shown in beige. C) Kernel density estimates for the difference between the up-going and down-going legs of fiber in each borehole D) Statistics describing the difference between down and up-going fibers for each borehole E) Average 3-standard-deviation noise for each borehole.

cavation on 27 May. The symmetry in the measurements between fiber legs is visually apparent. The depths at which the measurements are not symmetric typically coincide with depths where the fiber is expected to be poorly coupled to the rock mass, for example at the borehole collar or at the depths where grout is replaced by the resin plugs (beige bands, Figure 2B). But while the symmetry of the measurements between down and upgoing legs is evident, the absolute value measured at a given depth on either leg can vary significantly. This is likely a result of heterogeneous coupling of the fiber to grout and the grout to the rock mass. This could be the result of changes in the distribution of grout (e.g. air pockets) or to the effect of other equipment installed in the borehole. For example, in BCS-D5 the chain potentiometer might affect the strain measured on the fiber closest to it, but have less effect on the opposing leg. Also, for the inclined, grouted boreholes, the stress state may vary along the borehole circumference. In this case, fiber legs on opposing sides of the borehole could measure different responses to stress perturbation, even for the same depth in the borehole.

Figure 2C shows the difference between down and upgoing fiber measurements for all measurement times and channels, colored by borehole. The statistics for the distributions shown in Figure 2C are reported in Figure 2D. The fact that the distributions are nearly zero-mean signifies that there is no systematic preference for higher or lower values measured by one leg with respect to the other. The standard deviations of the curves in Figure 2D, however, range from 4.83 to 28.39 $\mu\epsilon$. This means that the measured strain at a given depth in a borehole might vary by tens of microstrains depending on which leg is selected, significantly increasing the uncertainty in the measured strain.

5.3 Measurement noise

We quantify the measurement noise following Madjdabadi et al. (2016). For each channel in a borehole, we calculate 3 standard deviations for a reference time period (with no expected strain signal). We then average this value over all channels in the sensor, resulting in a single noise value per borehole (Figure 2E). The noise levels range from 11.44 to 20.95 $\mu\epsilon$, meaning that each segment of the fiber cannot confidently resolve strains of less than these values.

5.4 Measurement artifacts

Two final artifacts are then removed from the data. The first artifact is an ambiguity in the exact position of each channel. The ambiguity arises because the channel location is reported at the center of the light pulse (for our tests either 0.5 or 1.0-m long). But the strain could be concentrated at any point (or points) inside the pulse. We follow Madjdabadi et al. (2016) and apply a realignment step detailed in the supplements.

The second artifact is a series of systematic shifts in the measured strain for all points in the fiber. These apparently correlate with shifts in the gain of the signal returned to the interrogator, although the two values should not be related. We undertook a process of removing these shifts for times where the gain also shifted. This process is also detailed in the supplements.

6 Results and discussion

6.1 DSS response to a local injection in a borehole

In the case of the PST, the change in pressure decay associated with FOP occurred at a pressure step of 4.8 MPa with a preceding step of 4.5 MPa, indicating that the FOP falls between these two pressures.

As mentioned in Section 3, the fibers in BCS-D1 and D2 are not grouted behind casing as in the other boreholes, instead they are anchored above the packers at the top of each injection and monitoring interval. Therefore, instead of reporting the true continuous measurements across the straddle packer intervals, we integrate the measurements along the boreholes between each anchor point, which gives the BCS-D1 displacement trace in Figure 3A a step-like appearance.

Figure 3A shows the measurement at 16:00 UTC on 12 June 2019 in BCS-D1. We measure the largest displacement (369 μm) at the 13–15 m injection interval, where the injection took place, and therefore where the applied fluid pressure was the largest.

Figure 3B shows the DSS and potentiometer time series at the top of the Main Fault in each borehole. The shaded area indicates a DITEST configuration with a spatial resolution of 0.5 m. The resolution was changed to 1.0 m after 14:06 UTC to reduce noise. The time series for the injection interval in BCS-D1 clearly shows extension of the fiber across the injection zone beginning at the onset of the pulse-step test, leveling off once the FOP is reached and a constant pressure state is imposed on the interval (4.5 MPa). The time resolution of our DSS configuration is approximately 10 minutes, similar to the duration of each pressure step, so we cannot resolve the expected deflation of the injection interval during pressure decay, with the exception of the final, 4.8 MPa pressure step (Figure 3B). The time series measurements at BCS-D2, D3, D4, and D5 slightly exceed the noise levels reported in Figure 2E, while the potentiometer measured no displacement in BCS-D5 during this test.

Nearly 300 μm was measured in the injection interval prior to reaching FOP, when deformation would be expected to occur in the fault zone due to the pressurized fluid forcing its way into the fault. Therefore, the DSS measurements prior to FOP probably reflect extension of the fiber by the pressurization of the straddle-packer interval. We plot the applied injection pressure versus the cumulative fiber optic strain at all pressure steps in Figure 3D. Prior to FOP, a 1 MPa increase in injection pressure resulted in approximately 139 μm of extension over the straddle packer assembly (dotted fit in Figure 3D). This pre-FOP behavior is of use in characterizing the strain response of the straddle-packer assembly and the borehole near-field effects during future injections.

Once FOP is reached and pressure diffuses into the fault zone, this relation becomes nonlinear and may reflect the fault hydromechanical response. If so, the rollover observed in the final two points in Figure 3D may indicate that fault opening has occurred. However, the peak pressure shown in Figure 3D is $\sim$4.34 MPa, lower than the 4.5–4.8 MPa indicated from the pressure data. The discrepancy between the pressure and strain data is likely due to the coarser temporal resolution of the DSS (one sample roughly every ten minutes). Because the pressure increase from 4.5 to 4.8 MPa occurs over less than one minute, the DSS cannot capture the exact FOP. In addition, the DSS measurement times don't correspond to exactly the time of the maximum pressure for each step, which lasts only briefly before decaying. This produces systematically lower pressures in Figure 3D relative to the maximum pressures applied at each step and may also contribute to the underestimate of FOP.

Away from the injection borehole, the fibers apparently detect a delayed deformation (extension) of the fault zone in D5 about one hour (after 16:00 UTC) after FOP is reached. D2, D3, and D4 are beneath the noise level, but correspond to a small contraction. These amount to $<50\ \mu\epsilon$ and can only be attributed to the fault zone with a low degree of confidence since they remain close to the noise level. Nevertheless, they tend to show that strain is propagating along the top of the fault from the injection interval. The contraction in D2 and D3 may indicate that, while no hydraulic connection has been made, stress has been transferred beyond the pressure front.

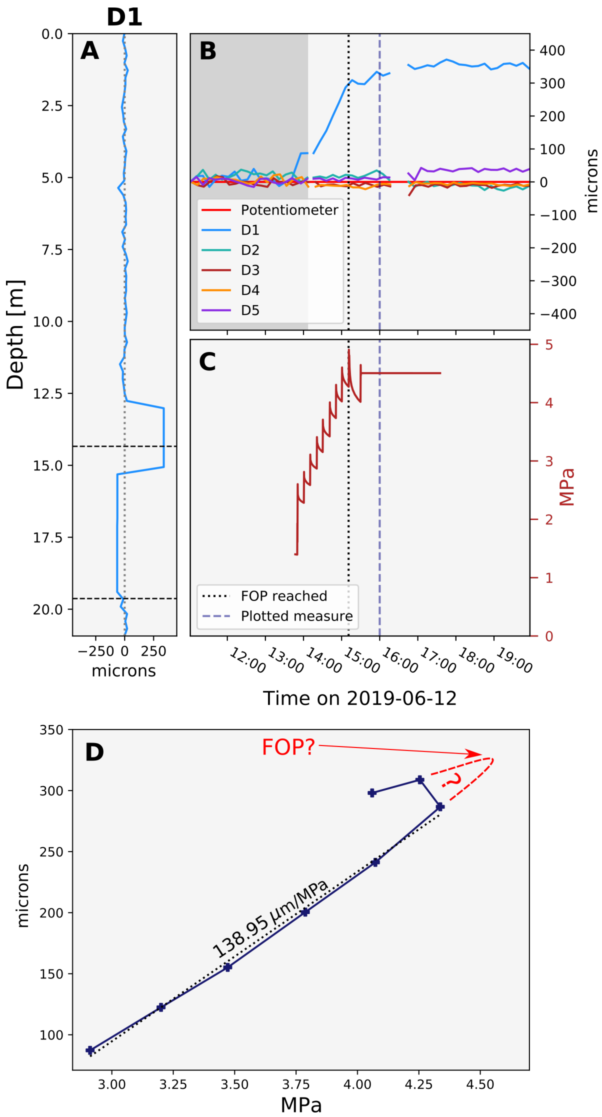

Figure 3. Signals recorded during the pulse-step test on 12 June 2019. A) DSS measurement at 15:30 UTC in BCS-D1. Vertical dotted line is zero strain and the horizontal dashed lines are the top and bottom of the Main Fault B) Time series of DSS measurement at the top of the Main Fault in each borehole. C) Injection pressure into the top of the Main Fault in D1. FOP was reached at the time of the dotted line. The dashed line indicates the time of the data plotted in panel A. D) Fiber displacement vs injection pressure in the BCS-D1 injection interval during the pulse test

6.2 DSS response to a remote stress transfer: gallery excavation

On 22 May 2019, the monitoring system began to record signals within the Main Fault zone (Figures 2 and 4) associated with the excavation of Gallery 18. From 23 May until the breakthrough on 27 May, there were three episodes of excavation, with the excavation front advancing between 1 and 3 m during each episode (Figure 4B, dotted line). Each episode induced movement on the Main Fault, rapid at the onset and decelerating towards a new steady state before accelerating again in response to the next excavation.

6.2.1 Comparison of DSS measurements to other instruments

In Figure 4A, we show both the chain potentiometer (red) and DSS measurements (purple) in BCS-D5 on 3 June 2019 following excavation breakthrough. The fracture density as estimated from analysis of drill core is shown in black. The potentiometer string has a variable spatial resolution defined by the spacing of the anchor points between individual elements. We plot these data as a series of steps to account for this. The spacing between elements is smallest across the Main Fault interval (0.5 m). Two other elements of roughly 8 m length are placed above the fault. At the depth of the Main Fault interval, the chain potentiometer and fiber optic measurements both clearly show that most of the movement within the fault interval is concentrated at the uppermost interface, where displacements of 282 μm and 210 μm are measured, respectively. A smaller magnitude peak is also observed at the bottom fault interface, respectively of 80 and 67 μm on the potentiometer and DSS. Above the fault, the DSS retains its 1 m spatial resolution, whereas the potentiometer averages displacements over two 8 meter intervals (from 11–19 m and 2–11 m). Two other large deformations are measured by the DSS; one just above the resin plug (16–17 m) and one at 8 m depth. The chain potentiometer, on the other hand, measures no displacement over its shallow intervals due to its lack of spatial resolution.

Figure 4B shows a time series comparison between the DSS and the potentiometer in BCS-D5. We integrated over the three potentiometer elements at 19.75, 20.25, and 20.75 m depths and did the same for the DSS across this depth interval to produce the displacement traces shown. The match between the two instruments is excellent, with a normalized cross correlation coefficient of 0.996 that, when combined with the match shown in Figure 4A, is an indication that the strain magnitudes measured by the DSS system are accurate (if we accept the industry standard potentiometer as a ground-truth). This shows that the DSS can accurately quantify the strain field, thereby complementing results from previous studies where DSS could be used only in a qualitative manner (Krietsch et al., 2018; Valley et al., 2012).

6.2.2 DSS sensitivity to shear

We also investigated the ability of the DSS system to detect shear displacement. Fiber optics are only able to measure changes along the axis of the fibers themselves (i.e. lengthening or shortening). In our case this means we can best resolve deformation of the rock mass which is oriented parallel to the axis of the boreholes. Obviously, the deformation field is not perfectly aligned with our fibers because it is typically localized on fractures and faults that will intersect our boreholes at oblique angles. This means that much of the movement we would like to measure will be oblique to the fiber optic sensor.

The SIMFIP instrument installed in BCS-D7 (see Section 3.0.3) measures the full three-dimensional displacement field across the Main Fault and therefore allows us a unique opportunity to estimate the amount of shear applied to the DSS fiber in BCS-D5. We first make the assumption that the displacement measured across the Main Fault at BCS-

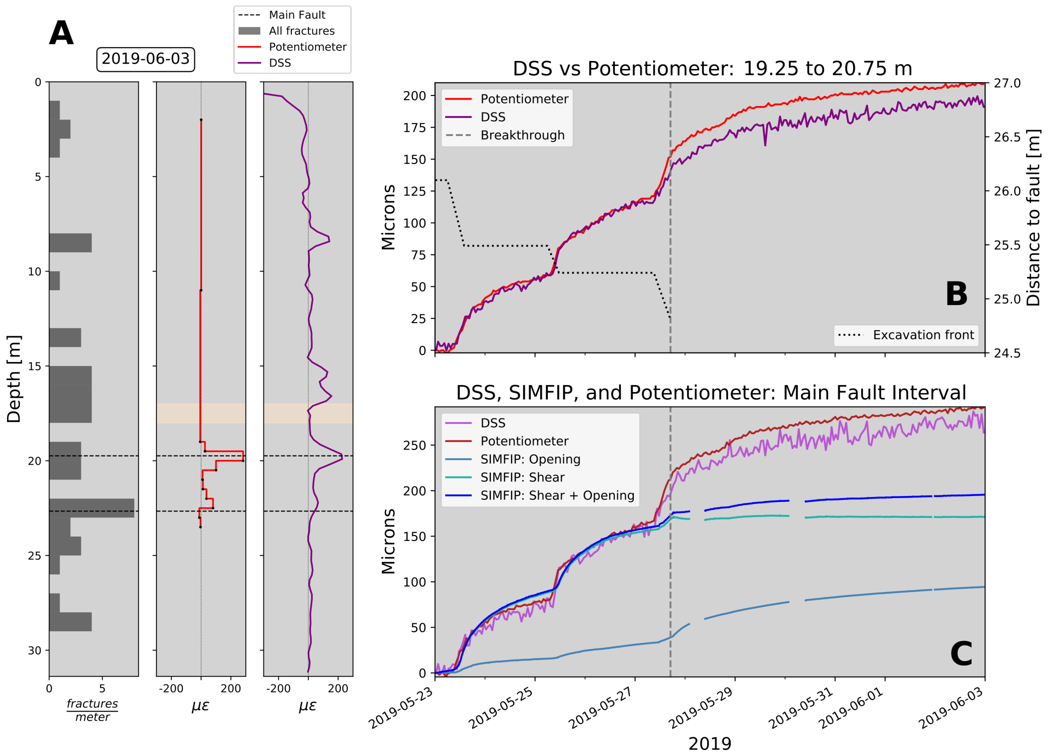

Figure 4. Fault response to gallery excavation - A) Comparison between fracture density, potentiometer extensional strain and DSS strain six days after the breakthrough of Gallery 18 at Niche CO_2. B) Time series comparison between DSS and potentiometer integrated between 19.25 and 20.75 m depth in D5. The dotted line shows the distance of the excavation front to the top of the fault at BCS-D5. The dashed line is the time of the breaktrough C) Potentiometer, DSS, and SIMFIP measurements over the fault zone. SIMFIP total shear is light green and borehole-parallel displacement is gray-blue. The dark blue curve shows the synthetic DSS measurement modeled from SIMFIP data.

D7 can be used as a proxy for displacement at BCS-D5, although the distance between the boreholes is roughly seven meters along the fault interface and the fault interface dips more steeply in D5 than in D7. We then rotate the SIMFIP-measured displacement tensor into the borehole coordinates of BCS-D5, such that one component is parallel to the borehole axis and the other two are perpendicular. We then compute the total displacement perpendicular to the borehole (i.e. total shear). We add the borehole-parallel and borehole-normal components of the rotated SIMFIP tensor (vector summation) to give the blue curve that is shown in Figure 4C. To directly compare this synthetic with the actual DSS and potentiometer measurements, we integrate both across the fault interval. The DSS and potentiometer curves in Figure 4C, still in excellent agreement when integrated across the fault, closely match the blue SIMFIP curve for the first two excavation 'pulses'. During these two periods, the SIMFIP recorded much more shear than normal-mode opening across the fault. This tells us that the DSS and potentiometer measurements are sensitive to more than simply borehole-parallel displacements, instead measuring almost all of the applied shear as well. However, for the final period of excavation, when the SIMFIP measured mostly normal-mode opening, the potentiometer and DSS measure much larger displacements. We suggest that the fault slips differently at its intersection with D5 than at its intersection with D7 and that we cannot simply assume the SIMFIP measurements accurately reflect movement even a few meters away. The surface of the Main Fault is actually quite complex. For example, the upper fault interface at D5 strikes N244^o and dips 81^{o}NW (possibly overturned) while in D7 it is more consistent with the overall Main Fault trend (strike N037^o, dip 64^{o}SE; Zappone et al., 2020). Although each patch has a similar strike, the opposite sense of dip may lead to different opening-mode behavior in response to the gallery excavation.

6.3 Distribution of deformations in and off the Main Fault

6.3.1 Off Main Fault deformation

Fiber-optic strains localize on a number of discrete features located outside the fault zone (Figure 5A). We divide these features into a shallow zone (<7 m depth) and a deep zone (>7 m depth, which includes the Main Fault). The deformations in the shallow zone are up to one order of magnitude larger than those measured below 7 meters depth. Figure 5B shows the measured strains in the upper 7 m of each borehole. Boreholes D3 and D5 show contractions of >800 and $\sim$600 $\mu\epsilon$, respectively. In contrast, D4 and D6 each show two smaller-magnitude peaks of extensional strain, each $\leq$200 $\mu\epsilon$. The differences between the shallow strains in each borehole indicate a complicated strain distribution in and around the intersection of Gallery 18 and niches "Sandwich" and CO_2 (Figure 1).

These likely reflect deformations within the 'excavation damage zone' (EDZ) commonly observed surrounding underground excavations (e.g. Blümling et al., 2007). The nature of the strain in the EDZ during excavation depends upon the geometrical relationship of the measuring point to the excavated zone. It is also controlled by the gallery trajectory with respect to in-situ stress state. For a horizontal tunnel in a normal faulting stress regime (sub-vertical $\sigma_1 > \sigma_{2,3}$, as at the MTRL), the top and bottom of the gallery should converge towards each other more than the sides (Corkum & Martin, 2007; Corkum, 2006).

However, the EDZ around the CS-D niche (where our boreholes are located) was likely already stable (Corkum & Martin, 2007) by the time of the Gallery 18 breakthrough detailed in this work. We are therefore observing the response of a stable, preexising EDZ as it merges with the new, unstable EDZ surrounding the approaching gallery excavation. The strains shown in Figure 5B are the result of complicated interactions between a new gallery and the preexisting galleries and niches, each with different orientations with respect to the far field stress (Figure 1C). This leads to a complicated redistribu-

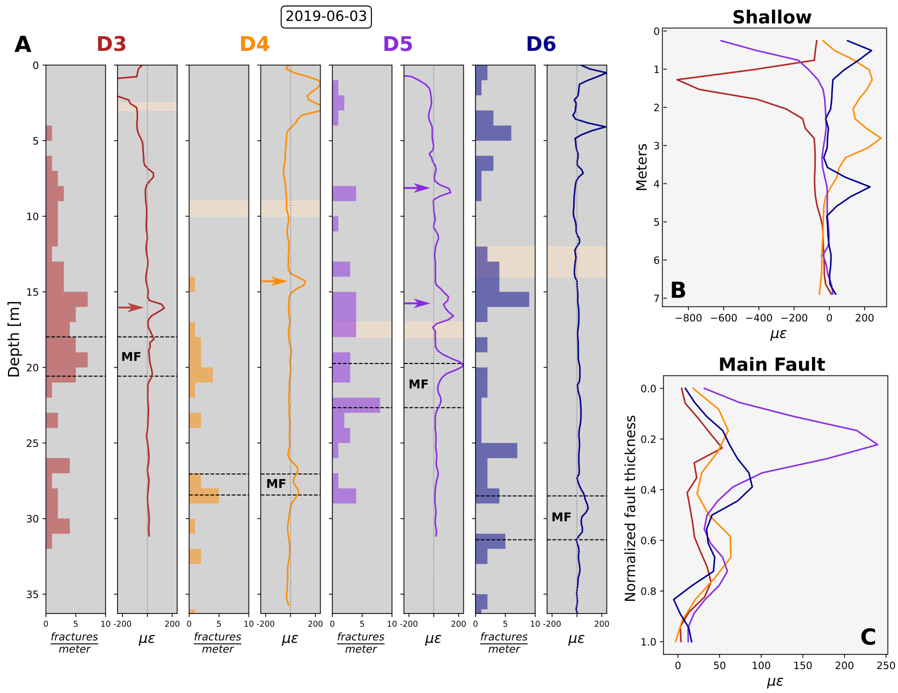

Figure 5. On and off-fault strains - A) Measured strain and fracture density estimated from core. D4 was drilled with destructive methods so we report fracture density from optical televiewer logs. Resin plugs are in beige, fault top and bottom are indicated by horizontal dotted lines. Arrows show above-fault features recorded on both the up and down-going fibers B) Strains for the upper 7 m of each borehole C) Strains within the fault zone for each borehole. Depths are normalized to the fault zone thickness in each borehole.

tion of the local stresses, resulting in extension in some locations (D4, D6) and contraction in others (D3, D5). D3 and D5 are drilled with similar orientations from opposing sides of Niche CO_2 and therefore show a similar shallow strain pattern. D4 and D6 were drilled through portions of the EDZ directly below a gallery and a niche, respectively. Given a vertical σ_1, where the roof and floor of the gallery should converge, it makes sense that D4 and D6 would show extension along the fiber axis. But apart from qualitative observations, a complicated modeling exercise will be required to shed more light on the patterns shown in Figure 5B.

Below five meters depth in all boreholes, strain is localized on several distinct features visible in Figure 5A (colored arrows). In boreholes D3, D4, and D5, at least one feature is present above the depth of the Main Fault (indicated by the dotted black lines), whereas in D6 the Main Fault itself is the only notable feature. In D3, D4, and D5, off-Main Fault deformations are >100 $\mu\epsilon$, comparable to and exceeding the strain measured within the Main Fault zone. About 18% of the off-Main Fault fractures identified in core logs correspond to the DSS features indicated by arrows in Figure 5A.

Geological interpretation of the core classifies the deepest non-fault feature in BCS-D3 (16 m depth) as an interval of scaly clay layers. Optical televiewer (OTV) images for D3 were too poor for accurate picking. The single shallow feature in D4, as identified in OTV logs, corresponds to a single fracture striking N052^o, dipping SE69^o. The 15–16-m depth interval in BCS-D5 is classified a distinct fault zone, four meters above the Main Fault (strikes N014–060^o, dips 20–70^{o}SE). The 8-meter anomaly in D5 corresponds to a series of features classified as either 'bedding' or 'fracture planes' in the core (strikes N053–082^o, dips 54–74^{o}SE). Unfortunately, due to the 1-meter spatial resolution, DSS anomalies cannot be assigned to any single feature where fracture density is >1 / meter (Figure 6).

6.3.2 Main Fault core deformation

Figure 5C shows the strains measured within the Main Fault zone for all boreholes. Because the thickness of the fault zone varies significantly between boreholes, we normalize the depths in order to better compare the distribution of strain within the fault core.

In all boreholes, strain localizes on the uppermost interface of the fault zone. In D5, $\sim$240 $\mu\epsilon$ accumulates on this surface, with lesser magnitudes in the other boreholes. This is explained by the closer location of D5 to the excavation front. Strain also localizes on the lower interface of the fault zone, with relatively little strain measured within the fault zone itself. This may indicate that the interfaces between fault zone and intact rock are the principal shear zones of the Main Fault. This is corroborated by core analysis that indicate up to 1 cm of black or gray fault gouge at the top and bottom of the fault zone (Wenning et al., 2020).

Compared to the other boreholes, strain in D6 (particularly on the upgoing fiber) appears more distributed over the entire fault zone. D6 is vertical and therefore oblique to the Main Fault. This makes it more sensitive to shear, which is better aligned with the fiber axis than in D3, D4, or D5. This could mean that D6 better captured small amounts of shear distributed within the entire fault zone than the other boreholes.

For the case of the gallery excavation, we suggest that slip on the upper Main Fault interface, being closer to the excavation, relieves some of the stress that otherwise would have been transmitted to the lower interface, thereby producing an apparent gradient. In addition, this stress shadow effect probably explains the lack of strain measured below the fault, even in the presence of identified fractures deeper in the boreholes.

7 Discussion

7.1 DSS ability to detect and characterize fault reactivation

We observed a break in the linear borehole strain response to injection once FOP was reached in BCS-D1 (Figure 3D). Such a break suggests that DSS can be used to locate, in time and space, features activated by fluid injection in a borehole. Our case study is limited by targeted injection using straddle packers, which predetermines the location of the fracture and the spatial resolution of the DSS system (due to anchoring across packer intervals). A simpler, and more powerful use of DSS in this context could involve pressurizing an entire borehole (or a long section) combined with fiber grouted behind perforated casing. In this scenario, a strain vs pressure curve like in Figure 3D could be plotted for each channel in the borehole. Without being anchored over a multi-meter interval (as with BCS-D1 here), a grouted fiber would then be capable of identifying the depth of any number of activated features, while pinpointing the pressure at which these features were activated.

We have also shown that DSS systems are sensitive to borehole shear displacement. For the first two excavation pulses in Figure 4C, DSS sensitivity to oblique slip was consistent with a simple vector sum of fault normal and shear displacement. While the reason for the discrepancy between the SIMFIP and DSS for the third phase is unclear, it is potentially a result of variations in Main Fault orientation. While we were partly successful in modeling the measured DSS using the nearby SIMFIP signal, DSS measurements would be much more powerful if fault-normal and shear displacement (where shear often far exceeds normal strain) could be parsed without the need for independent, downhole instruments. One possible approach could be to conduct a slip tendency analysis of the fractures that display deformation on the DSS (similar to Figure 6). Given a most likely slip vector on a plane with known orientation, it should be possible to estimate the amount of normal versus shear displacement required to best fit the DSS measurements.

7.2 Implications for fault reactivation in a shale caprock

DSS signals during the Gallery 18 excavation display localized peaks at the top and bottom of the Main Fault zone, but also at off-fault depths in the hanging wall. The 16-m anomaly in D3 displays nearly twice the displacement of the top or bottom interfaces of the Main Fault. In addition, the anomalies in D4 and D5 display similar deformation magnitudes to the Main Fault zone. This indicates that a caprock's strain response to remote stress perturbation is definitely not continuous and it can localize on less-easily identified, but distinct structures than large fault zones such as the Main Fault. Core reveals that the Main Fault interfaces show development of fault gouge and scaly clay, indicating significant amounts of past slip. But so do the 16-meter anomalies in D3 and D5, further hinting at Main Fault-amounts of slip on these lesser structures under tectonic loading conditions.

The degree to which a discontinuity will respond to remote stress transfer depends entirely on its orientation relative to both the far-field stress and the direction of the stress transfer (Handin, 1969; Freed, 2005). Figure 6 shows each plane identified in the BCS-D4, D5, and D6 optical televiewer logs colored by slip tendency (increasing from blue to red) when subjected to the stress field determined by Guglielmi et al. (2020) for the MTRL. The planes are divided into three categories: Main Fault zone features (6A), features that correlate with a measured strain on DSS (6B), and features that displayed little-to-no strain (6C). As detailed by Wenning et al. (2020), the Main Fault zone comprises a variety of fracture sets of varying orientations, including fault-zone parallel fractures and WNW-dipping conjugate fractures, which are the most prone to slip of any of the identified features (red features, Figure 6A). As we mentioned above, however, slip seemed to localize on the upper and lower fault zone interfaces, which are much further from failure in the in situ stress conditions (dashed black lines and adjacent green lines, Figure 6), indicating that the excavation probably induced a large change in the local stress field, possibly affecting mostly the features oriented similarly to the fault zone.

The off-fault fractures predominantly strike NE, with dips ranging from $\sim$10–70^o (Figure 6B-C). As with the Main Fault interfaces, these features are invariably far from being critically stressed (10s of MPa) in the pre-excavation stress field. In a static stress state, the features that displayed a DSS signal are no more likely to slip than those which showed no deformation, making it difficult to discern, a priori, solely from OTV logs which features would be most likely to slip. These sets of features also span the orientation of both bedding and the Main Fault zone, meaning we cannot state whether one or the other is hosting the deformation that is being measured. However, this may be an effect of the DSS spatial resolution, which prevents us from assigning strain to single features and may obscure subtle variations between slipping and non-slipping features. Because the induced stress perturbation decreases with distance from the excavation, we color each feature in the lower row of Figure 6 by its distance from the breakthrough point. The features in column B, associated with strain signals outside the fault zone, are closer (on average, shown by their lighter color) to the excavation front than either the Main Fault itself, or the features displaying no strain. This suggests that, for features outside the weak fault zone, the distance to the stress perturbation is a main controlling factor in whether they accommodate deformation. As we would expect, those further away are less likely to be reactivated.

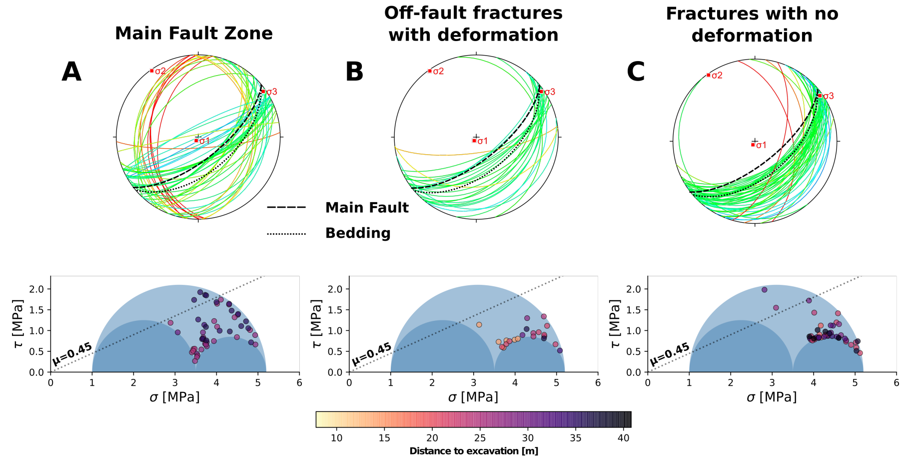

Figure 6. Fractures identified in optical televiewer logs in BCS-D4, D5, and D6 - A) Within the Main Fault zone B) outside of the Main Fault but displaying deformation on DSS C) All other fractures. The upper plots are lower hemisphere projections of poles and planes, colored by slip tendency in the local stress regime estimated by Guglielmi et al. (2020) (blue=low, red=high tendency). Dotted line shows the orientation of bedding at the MTRL, the dashed line shows the approximate orientation of the Main Fault. The lower row plots show the state of stress on each fracture relative to a Mohr Coulomb failure envelope for cohesionless fractures. Following Orellana et al. (2018), a peak coefficient of friction of μ=0.45 is used. The color of each dot corresponds to the distance from the feature to the excavation front (light=closer, dark=further).

Careful characterization of the core offers an additional clue as to which features are most prone to slip. With the exception of the 8-m anomaly in D5, the features that displayed significant strain exhibited either an accumulation of scaly clay, fault gouge, or a high degree of fracturing. Therefore, despite the limited number of slipping fractures and their similar orientations to many other features, it may be possible to identify zones of potential caprock deformation in advance via signs of slip identified in the drilling core.

8 Conclusions

We presented measurements from seven boreholes intersecting a fault zone in clay rock at the Mont Terri Rock Laboratory in Switzerland. Our dataset comprises two periods of differing-magnitude stress perturbation on the fault, allowing us to verify the ability of our distributed fiber system to detect various magnitudes of displacement. Importantly, one chain potentiometer and one high-resolution 3D displacement sensor, installed alongside the fibers, allowed us to corroborate the magnitudes of the strain measurements made via DSS with independent systems.

We analyzed a pulse-step injection test into the top of the Main Fault with a maximum pressure of 4.8 MPa. Fiber installed across the injection interval of BCS-D1 detected >300 μm of extension associated with injection, while measurements from other boreholes indicated <50 μm of deformation (up to 5 m from injection along the fault interface). Measured strain within the injection interval was affected by pressurization of the straddle packer assembly and deformation of the fault. Prior to reaching fault opening pressure (~4.5 MPa), strain increased linearly with injection pressure, likely due to lengthening of the injection interval. Once FOP was reached, however, the strain vs pressure curve deviated from the linear trend, indicating a response from the rock. The break from this trend occurs after 4.3 MPa, lower than hydraulic data suggest for FOP, but the DSS may have too low a temporal resolution to resolve the exact FOP for this case. This method of identifying fracture activation may be most useful when combined with fiber-behind-casing installations and large injection intervals (10s of meters). In such a scenario, hydraulic data would be complemented by DSS, which would be able to identify the activation of multiple fractures within the same injection interval.

During excavation of a new gallery at Mont Terri, located about 30 m away from our instrumented boreholes, strains ranging from 50–240 $\mu\epsilon$ were measured mainly at the top and bottom of the fault zone at each of our boreholes, well above the maximum 3σ noise level of $\sim$20 $\mu\epsilon$. We showed that the DSS measurement has a significant sensitivity to shear strain in a grouted borehole and thus can be used as a proxy to estimate fault slip. The complex mechanical response of the gallery excavation damage zone was also captured on the DSS. Indeed, our tuned measurements also provide insight into the reactivation behavior of a clay-hosted fault.

The DSS measurements show that deformation in the rock mass localized on several discrete fractures identified in core and logs. Within the Main Fault, deformation concentrated on the upper and lower fault zone interfaces, with relatively little deformation occurring inside the fault zone. Core revealed similar zones of fault gouge on these interfaces, suggesting similar amounts of slip. Therefore, the greater strain we measured on the upper interface probably reflects a stress shadowing effect whereby slip on the upper interface relieved some of the stress change that otherwise would have reached the lower interface. Away from the fault, deformation concentrated on features with a similar orientation and slip tendency to the Main Fault itself. Most such fractures identified in OTV logs were not reactivated, but those that did slip were unique in displaying signs of past slip in the drilling core and were therefore identifiable as potential zones of slip concentration prior to injection.

Previous grouted DSS measurements have only proven to be of qualitative use. In contrast to these previous studies, we show how a grouted network of fiber optic cables can complement other monitoring systems to quantify the subsurface strain field. While additional case studies like ours are necessary to expand the existing understanding of these fiber optic measurements, they should prove useful in monitoring rock mass movements in many energy and geotechnical applications. Taking our network of boreholes intersecting a fault as an example, similar systems at Mont Terri and in other settings could be valuable in constraining the 2- and 3-D strain field near faults and fractures and can therefore help fill in our understanding of the spectrum of slip behavior that eventually culminates in induced seismicity.

Acknowledgments

The authors are deeply grateful to the partners of the Mont Terri Project that contributed to the funding of the CS-D and FS-B experiments: the Swiss Federal Office of Topography (Swisstopo), the Swiss Federal Nuclear Safety Inspectorate (ENSI), the Japanese Atomic Energy Agency (JAEA), the Institute of Radioprotection and of Nuclear Safety (IRSN, France), TOTAL SE, CHEVRON, the Federal Institute for Geosciences and Natural Resources (BGR, Hannover), the Swiss Federal Institute of Technology (ETH Zurich), and the U.S. Department of Energy. The Mont Terri Project is an international research project for the hydrogeological, geochemical, and geotechnical characterizations of a clay formation (Opalinus Clay). Funding for Berkeley Lab's analysis of the FS-B data described in this study was provided by the Assistant Secretary for Fossil Energy as part of the Core Carbon Storage and Monitoring Research (CCSMR) and National Risk Assessment Partnership (NRAP) programs of the U.S. Department of Energy under contract FP00007630. Experimental data are available in the supporting information. The CS-D experiment is part of the ACT ELEGANCY, Project No 271498. This project is supported by the Pilot and Demonstration Programme of the Swiss Federal Office of Energy (SFOE).

The stereonet and Mohr-Coulomb plots for Figure 6 were generated using Rick Allmendinger's software packages Stereonet and MohrPlotter, found here: https://www.rickallmendinger.net (Allmendinger et al., 2011).

Access to the datasets presented in this paper will be made available via a public server at ETH Zurich prior to acceptance of this manuscript.

References

Allmendinger, R. W., Cardozo, N., & Fisher, D. M. (2011). *Structural Geology Algorithms*. Cambridge University Press. Retrieved from `https://doi.org/10.1017%2Fcbo9780511920202` doi: 10.1017/cbo9780511920202

Birkholzer, J. (2018). Can Induced Seismicity Cause Fault Leakage and How Does it Evolve with Time? In *14th greenhouse gas control technologies conference melbourne* (pp. 21–26).

Blümling, P., Bernier, F., Lebon, P., & Martin, C. D. (2007, jan). The excavation damaged zone in clay formations time-dependent behaviour and influence on performance assessment. *Physics and Chemistry of the Earth Parts A/B/C*, *32*(8-14), 588–599. Retrieved from `https://doi.org/10.1016%2Fj.pce.2006.04.034` doi: 10.1016/j.pce.2006.04.034

Bossart, P., Bernier, F., Birkholzer, J., Bruggeman, C., Connolly, P., Dewonck, S., … Wieczorek, K. (2017, dec). Mont Terri rock laboratory 20 years of research: introduction, site characteristics and overview of experiments. In *Mont terri rock laboratory, 20 years* (pp. 3–22). Springer International Publishing. Retrieved from `https://doi.org/10.1007%2F978-3-319-70458-6_1` doi: 10.1007/978-3-319-70458-6_1

Corkum, A. (2006). Non-linear behaviour of opalinus clay around underground excavations..

Corkum, A., & Martin, C. (2007, sep). Modelling a mine-by test at the Mont Terri rock laboratory Switzerland. *International Journal of Rock Mechanics and Mining Sciences*, *44*(6), 846–859. Retrieved from `https://doi.org/10.1016%2Fj.ijrmms.2006.12.003` doi: 10.1016/j.ijrmms.2006.12.003

Delepine-Lesoille, S., Phéron, X., Bertrand, J., Pilorget, G., Hermand, G., Farhoud, R., … Lanticq, V. (2012). Industrial Qualification Process for Optical Fibers Distributed Strain and Temperature Sensing in Nuclear Waste Repositories. *Journal of Sensors*, *2012*, 1–9. Retrieved from `https://doi.org/10.1155%2F2012%2F369375` doi: 10.1155/2012/369375

Freed, A. M. (2005, may). EARTHQUAKE TRIGGERING BY STATIC DYNAMIC AND POSTSEISMIC STRESS TRANSFER. *Annual Review of Earth and Planetary Sciences*, *33*(1), 335–367. Retrieved from `https://doi.org/10.1146%2Fannurev.earth.33.092203.122505` doi: 10.1146/annurev.earth.33.092203.122505

Guglielmi, Y., Birkholzer, J., Rutqvist, J., Jeanne, P., & Nussbaum, C. (2017, jul). Can Fault Leakage Occur Before or Without Reactivation? Results from an in Situ Fault Reactivation Experiment at Mont Terri. *Energy Procedia*, *114*, 3167–3174. Retrieved from `https://doi.org/10.1016%2Fj.egypro.2017.03.1445` doi: 10.1016/j.egypro.2017.03.1445

Guglielmi, Y., Cappa, F., Lançon, H., Janowczyk, J. B., Rutqvist, J., Tsang, C. F., & Wang, J. S. Y. (2013). ISRM Suggested Method for Step-Rate Injection Method for Fracture In-Situ Properties (SIMFIP): Using a 3-Components Borehole Deformation Sensor. In *The ISRM suggested methods for rock characterization testing and monitoring: 2007-2014* (pp. 179–186). Springer International Publishing. Retrieved from `https://doi.org/`

10.1007%2F978-3-319-07713-0_14 doi: 10.1007/978-3-319-07713-0_14

Guglielmi, Y., Nussbaum, C., Jeanne, P., Rutqvist, J., Cappa, F., & Birkholzer, J. (2020, feb). Complexity of Fault Rupture and Fluid Leakage in Shale: Insights From a Controlled Fault Activation Experiment. *Journal of Geophysical Research: Solid Earth*, *125*(2). Retrieved from https://doi.org/10.1029%2F2019jb017781 doi: 10.1029/2019jb017781

Guglielmi, Y., Nussbaum, C., Robertson, M., Ajo-Franklin, J., Zappone, A., Kloppenburg, A., & Birkholzer, J. (2018). *FS-B Experiment: Imaging the long-term loss of faulted host rock integrity - Test plan, Mont Terri Technical Note* (Tech. Rep. No. TN2018-20).

Handin, J. (1969, oct). On the Coulomb-Mohr failure criterion. *Journal of Geophysical Research*, *74*(22), 5343–5348. Retrieved from https://doi.org/10.1029%2Fjb074i022p05343 doi: 10.1029/jb074i022p05343

Hartog, A. H. (2017). *An Introduction to Distributed Optical Fibre Sensors.* CRC Press. Retrieved from https://doi.org/10.1201%2F9781315119014 doi: 10.1201/9781315119014

Horiguchi, T., & Tateda, M. (1989). BOTDA-nondestructive measurement of single-mode optical fiber attenuation characteristics using Brillouin interaction: theory. *Journal of Lightwave Technology*, *7*(8), 1170–1176. Retrieved from https://doi.org/10.1109%2F50.32378 doi: 10.1109/50.32378

Hostettler, B., Reisdorf, A. G., Jaeggi, D., Deplazes, G., Bläsi, H., Morard, A., ... Menkveld-Gfeller, U. (2017, feb). Litho- and biostratigraphy of the Opalinus Clay and bounding formations in the Mont Terri rock laboratory (Switzerland). *Swiss Journal of Geosciences*, *110*(1), 23–37. Retrieved from https://doi.org/10.1007%2Fs00015-016-0250-3 doi: 10.1007/s00015-016-0250-3

Iten, M., Puzrin, A. M., & Schmid, A. (2008, mar). Landslide monitoring using a road-embedded optical fiber sensor. In W. Ecke, K. J. Peters, & N. G. Meyendorf (Eds.), *Smart sensor phenomena technology, networks, and systems 2008.* SPIE. Retrieved from https://doi.org/10.1117%2F12.774515 doi: 10.1117/12.774515

Jaeggi, D., Laurich, B., Nussbaum, C., Schuster, K., & Connolly, P. (2017, jan). Tectonic structure of the "Main Fault" in the Opalinus Clay Mont Terri rock laboratory (Switzerland). *Swiss Journal of Geosciences*, *110*(1), 67–84. Retrieved from https://doi.org/10.1007%2Fs00015-016-0243-2 doi: 10.1007/s00015-016-0243-2

jun Wang, B., Li, K., Shi, B., & qing Wei, G. (2008, sep). Test on application of distributed fiber optic sensing technique into soil slope monitoring. *Landslides*, *6*(1), 61–68. Retrieved from https://doi.org/10.1007%2Fs10346-008-0139-y doi: 10.1007/s10346-008-0139-y

Krietsch, H., Gischig, V., Jalali, M., Doetsch, J., Valley, B., Amann, F., et al. (2018). A comparison of FBG-and Brillouin-strain sensing in the framework of a decameter-scale hydraulic stimulation experiment. In *52nd us rock mechanics/geomechanics symposium.*

Madjdabadi, B., Valley, B., Dusseault, M., & Kaiser, P. (2014). Numerical study of grout–rock mass interaction effect on distributed optical fibre sensor measurements. In *Proceedings of the seventh international conference on deep and high stress mining.* Australian Centre for Geomechanics Perth. Retrieved from https://doi.org/10.36487%2Facg_rep%2F1410_31_madjdabadi doi: 10.36487/acg_rep/1410_31_madjdabadi

Madjdabadi, B., Valley, B., Dusseault, M. B., & Kaiser, P. K. (2016, jan). Experimental evaluation of a distributed Brillouin sensing system for measuring extensional and shear deformation in rock. *Measurement*, *77*, 54–66. Retrieved from https://doi.org/10.1016%2Fj.measurement.2015.08.040 doi: 10.1016/j.measurement.2015.08.040

Naruse, H. (1999, sep). River levee strain measurement using fiber optic distributed strain sensor. In *13th international conference on optical fiber sensors.* SPIE. Retrieved from https://doi.org/10.1117%2F12.2302056 doi: 10.1117/12.2302056

Naruse, H., Komatsu, K., Fujihashi, K., & Okutsu, M. (2005, may). Telecommunications tunnel monitoring system based on distributed optical fiber strain measurement. In *17th international conference on optical fibre sensors.* SPIE. Retrieved from https://doi.org/10.1117%2F12.623645 doi: 10.1117/12.623645

Nussbaum, C., Bossart, P., Amann, F., & Aubourg, C. (2011, sep). Analysis of tectonic structures and excavation induced fractures in the Opalinus Clay Mont Terri underground rock laboratory (Switzerland). *Swiss Journal of Geosciences*, *104*(2), 187–210. Retrieved from https://doi.org/10.1007%2Fs00015-011-0070-4 doi: 10.1007/s00015-011-0070-4

Orellana, L., Scuderi, M., Collettini, C., & Violay, M. (2018). Frictional properties of opalinus clay: Implications for nuclear waste storage. *Journal of Geophysical Research: Solid Earth*, *123*(1), 157–175.

Rinaldi, A. P., Guglielmi, Y., Zappone, A., Soom, F., Robertson, M., Cook, P., ... Nussbaum, C. (2020, mar). Coupled processes in clay during tunnel excavation. Copernicus GmbH. Retrieved from https://doi.org/10.5194%2Fegusphere-egu2020-18041 doi: 10.5194/egusphere-egu2020-18041

Sun, Y., Xue, Z., Hashimoto, T., Lei, X., & Zhang, Y. (2020, jan). Distributed Fiber Optic Sensing System for Well-Based Monitoring Water Injection Tests—A Geomechanical Responses Perspective. *Water Resources Research*, *56*(1). Retrieved from https://doi.org/10.1029%2F2019wr024794 doi: 10.1029/2019wr024794

Tateda, M., Horiguchi, T., Kurashima, T., & Ishihara, K. (1990). First measurement of strain distribution along field-installed optical fibers using Brillouin spectroscopy. In *Optical fiber communication.* OSA. Retrieved from https://doi.org/10.1364%2Fofc.1990.pd15 doi: 10.1364/ofc.1990.pd15

Valley, B., Madjdabadi, B. M., Kaiser, P. K., Dusseault, M. B., et al. (2012). Monitoring mining-induced rock mass deformation using distributed strain monitoring based on fiber optics. In *Isrm international symposium-eurock 2012.*

Wenning, Q. C., Madonna, C., Zappone, A., Grab, M., Rinaldi, A. P., Plötze, M., ... Wiemer, S. (2020). Shale fault zone structure and stress dependent anisotropic permeability and seismic velocity properties (opalinus clay, switzerland). *Journal of Structural Geology*, 104273.

Zappone, A., Rinaldi, A. P., Grab, M., Wenning, Q., Roques, C., Madonna, C., ... others (2020). Fault sealing and caprock integrity for co 2 storage: an in-situ injection experiment. *Solid Earth Discussions*, 1–51.

Zhang, C.-C., Shi, B., Gu, K., Liu, S.-P., Wu, J.-H., Zhang, S., ... Wei, G.-Q. (2018, nov). Vertically Distributed Sensing of Deformation Using Fiber Optic Sensing. *Geophysical Research Letters*, *45*(21), 11,732–11,741. Retrieved from https://doi.org/10.1029%2F2018gl080428 doi: 10.1029/2018gl080428

Zhang, Z., Fang, Z., Stefani, J., DiSiena, J., Bevc, D., Ning, I. L. C., ... Tan, Y. (2020, aug). Modeling of Fiber Optic Strain Responses to Hydraulic Fracturing. *GEOPHYSICS*, 1–22. Retrieved from https://doi.org/10.1190%2Fgeo2020-0083.1 doi: 10.1190/geo2020-0083.1

Zhou, Z., He, J., Huang, M., He, J., Ou, J., & Chen, G. (2010, mar). Casing pipe damage detection with optical fiber sensors: a case study in oil well constructions. In P. J. Shull, A. A. Diaz, & H. F. Wu (Eds.), *Nondestructive characterization for composite materials aerospace engineering, civil infrastructure, and homeland security 2010.* SPIE. Retrieved from https://doi.org/10.1117%2F12.848727 doi: 10.1117/12.848727